AIAA JOURNAL
Vol. 34, No. 2, February 1996

Using High-Order Accurate Essentially Nonoscillatory Schemes for Aeroacoustic Applications

Jay Casper*
ViGYAN, Inc., Hampton, Virginia 23666
and
Kristine R. Meadows†
NASA Langley Research Center, Hampton, Virginia 23681

The numerical study of aeroacoustic problems places stringent demands on the choice of a computational algorithm, particularly when shock waves are involved. Because of their dual capacity for high-order accuracy and high-resolution shock capturing, the recently developed class of essentially nonoscillatory (ENO) schemes has generated considerable interest in regard to such problems. The use of ENO schemes for aeroacoustic applications is investigated, with particular attention to the control of the adaptive stenciling procedure. A modification of previously developed stencil-biasing procedures is proposed. This nonlinear stencil biasing allows a freer adaptation near discontinuities than is allowed by the previous biasing methods, without disturbing the biased, stable stencils that are desired in smooth regions. The accuracy of these new methods is validated through the study of a shocked nozzle flow. An axisymmetric shock-vortex interaction is then investigated. Numerical results indicate a reduction in error when compared with results in which other stencil-biasing procedures are used.

Nomenclature

A	= nozzle area
E	= total specific energy
h	= computational mesh width
M	= Mach number
n	= order of accuracy
P	= pressure
$\mathcal{P}_i$	= local polynomial approximation
$\mathcal{R}$	= polynomial approximation operator
r	= radial distance from axis of symmetry
S	= entropy, P/ρ^γ
T_δ	= time-scale unit, δ/u
u, v	= velocity components
γ	= ratio of specific heats
δ	= vortex core radius
$\epsilon, \bar{\sigma}$	= stencil-biasing parameters
θ^k	= stencil-biasing switch
κ	= circulation
ρ	= density
Ψ	= stream function

Introduction

THIS work is motivated by the desire to develop numerical methods that will be useful in the study of aeroacoustic phenomena that occur in shocked flows. For example, the presence of shocks in jet flows, on airfoils, and in supersonic combustion inlets contributes significantly to sound generation. Problems such as these represent some of the more challenging aspects of the ongoing research in the developing area of computational aeroacoustics (CAA).

The desire to obtain acoustic information from a numerical solution that involves shock waves is a demanding proposition for a computational algorithm. High-order accuracy is required for the propagation of high-frequency, low-amplitude waves. In addition, high resolution of discontinuities is desired, without spurious oscillations that can degrade the solution. The class of essentially nonoscillatory (ENO) shock-capturing schemes[1,2] has been designed to have such properties. In this work, it is intended to demonstrate the usefulness of these schemes and to suggest some modifications that will make them more robust with regard to CAA problems that involve shock waves.

The dual capacity of ENO schemes for high-order accuracy and nonoscillatory shock-capturing is achieved through the use of adaptive stenciling. That is, the local polynomial approximation operator adapts its interpolation set to the smoothest available part of the solution. In this way, ENO schemes can approximate the smooth regions of a piecewise continuous function to high-order accuracy without the oscillatory behavior that is associated with interpolation across steep gradients. Furthermore, adaptive stenciling enables high-resolution shock capturing. Although these properties are desirable, previous research has shown that the accuracy of these schemes can degenerate when the stencils are allowed to freely adapt.[3] Further research indicates that this accuracy problem can be remedied by biasing the stencils toward those that are linearly stable.[4–6] However, as will be shown in a present test case, spurious errors can occur when this biasing is implemented in a problem with moving discontinuities. Such results demonstrate the need for further consideration in regard to the adaptive stenciling procedure.

The following two sections briefly describe the ENO schemes employed in this work, with particular attention paid to the adaptive stenciling algorithm. The previously developed methods for constraining this adaptation through the use of biasing parameters are discussed. A modification to this stencil biasing is proposed and tested on the solution of a shocked flow in a quasi-one-dimensional nozzle. The numerical method is then applied to the interaction of a vortex and a shock wave in an axisymmetric flow. Numerical results for this problem, obtained from various modifications of the numerical scheme, are compared. Concluding remarks are made in the final section.

Numerical Method

For the sake of brevity, the necessary details of the ENO schemes

Presented as Paper 95-0163 at the AIAA 33rd Aerospace Sciences Meeting, Reno, NV, Jan. 9–12, 1995; received Jan. 30, 1995; revision received Aug. 16, 1995; accepted for publication Aug. 21, 1995.

*Research Engineer, Advanced Technology Group, 30 Research Drive; currently Research Assistant Professor, Department of Aerospace Engineering, Old Dominion University, Norfolk, VA 23529.
†Aerospace Engineer, Fluid Mechanics and Acoustics Division.

to be used in this work are presented within the context of a one-dimensional scalar equation,

$$\frac{\partial}{\partial t}U + \frac{\partial}{\partial x}F(U) = 0 \tag{1}$$

A control-volume formulation is obtained by integrating Eq. (1) on an interval $[x_{i-1/2}, x_{i+1/2}]$ with center x_i and volume Δx_i. The conservation law can then be written

$$\frac{\partial}{\partial t}\bar{U}_i(t) = \frac{-1}{\Delta x_i}\left\{F\left[U\left(x_{i+\frac{1}{2}}, t\right)\right] - F\left[U\left(x_{i-\frac{1}{2}}, t\right)\right]\right\} \tag{2}$$

where

$$\bar{U}_i(t) = \frac{1}{\Delta x_i}\int_{x_{i-\frac{1}{2}}}^{x_{i+\frac{1}{2}}} U(x,t)\,dx \tag{3}$$

is the cell average of U on the ith interval at time t. Temporal integration of Eq. (2) can be accomplished by a method-of-lines approach. In particular, the Runge–Kutta methods of Shu and Osher[2] will be used. The right-hand side of Eq. (2) is approximated in a manner similar to that introduced by Harten et al.[1]; a brief description follows.

To approximate the fluxes in Eq. (2) to high-order accuracy, the spatial operator must include a high-order pointwise approximation to $U(x,t)$. However, at a given time t, only the cell averages in Eq. (3) are available. Therefore, a pointwise reconstruction of the solution from its cell averages is required. To this end, let $\mathcal{R}$ be an operator that reconstructs the cell averages and yields a piecewise polynomial $\mathcal{R}[x; \bar{U}(t)]$ of degree $n-1$ that approximates $U(x,t)$ to high order, wherever $U(x,t)$ is sufficiently smooth. This operator $\mathcal{R}$ acts in a piecewise manner in that the solution is locally reconstructed within each cell. Let $\mathcal{P}_i$ denote the polynomial of degree $n-1$ that approximates $U(x,t)$ in the ith cell, at time t, i.e.,

$$\begin{aligned}\mathcal{P}_i(x) &\equiv \mathcal{R}[x; \bar{U}(t)], \qquad x_{i-\frac{1}{2}} \le x \le x_{i+\frac{1}{2}} \\ &= U(x,t) + \mathcal{O}(h^n)\end{aligned} \tag{4}$$

where $h = \max_i\{\Delta x_i\}$. The specific method used in this work is the reconstruction by primitive proposed by Harten et al.[1] and is not detailed here.

This piecewise reconstruction can cause jumps in the approximate solution at the cell interfaces that are $\mathcal{O}(h^n)$ in smooth regions and $\mathcal{O}(1)$ near discontinuities. The fluxes in Eq. (2) are then approximated by solving the local Riemann problems at the cell interfaces. Thus, the right-hand side of Eq. (2) is replaced by its high-order approximation, which yields

$$\frac{\partial}{\partial t}\bar{U}_i(t) = \frac{-1}{\Delta x_i}\left[\hat{F}_{i+\frac{1}{2}}(t) - \hat{F}_{i-\frac{1}{2}}(t)\right] \tag{5a}$$

where

$$\hat{F}_{i+\frac{1}{2}}(t) = F^{Rm}\left[\mathcal{P}_i\left(x_{i+\frac{1}{2}}\right), \mathcal{P}_{i+1}\left(x_{i+\frac{1}{2}}\right)\right] \tag{5b}$$

and $F^{Rm}(U_L, U_R)$ denotes the flux that is associated with the solution of the Riemann problem whose initial states are U_L and U_R. Upon temporal integration of Eq. (5a) with an appropriately high-order Runge–Kutta method,[2] the scheme in Eq. (5) is locally nth-order accurate in the L_1 sense. (See Ref. 1 for details.) The extensions of these schemes to hyperbolic systems and multiple spatial dimensions can be found in Refs. 1 and 7.

Adaptive Stenciling

The most unique aspect of the reconstruction operator $\mathcal{R}$ is its use of adaptive stenciling. That is, the interpolation set used for the approximation of $U(x,t)$ within a given cell is allowed to shift in an attempt to use the smoothest possible information. This adaptive stenciling makes ENO schemes highly nonlinear and is the focus of their application in this paper.

To determine a local polynomial $\mathcal{P}_i$ of degree $n-1$ within the ith cell, information from n cell averages is required, including $\bar{U}_i$ itself and $n-1$ of its neighbors. Let $j^n(i)$ denote the leftmost index of the stencil that is used to locally determine the polynomial of degree $n-1$ in $[x_{i-1/2}, x_{i+1/2}]$. The index $j^n(i)$ is determined in a hierarchical manner. Cells are annexed to the interpolation set based on local smoothness criteria. Information about the smoothness of the solution on a given stencil is obtained from the local differences of the cell averages on that stencil. Let Δ_i^k denote the operator that yields the kth forward difference on a stencil of $k+1$ cells with leftmost index i, which is defined recursively by

$$\Delta_i^1\bar{U} = \bar{U}_{i+1} - \bar{U}_i$$

$$\Delta_i^k\bar{U} = \Delta_{i+1}^{k-1}\bar{U} - \Delta_i^{k-1}\bar{U}, \qquad k = 2, 3, \ldots$$

The algorithm begins by setting $j^1(i) = i$. To choose $j^{k+1}(i)$, $k = 1, \ldots, n-1$, the two stencils considered as candidates are those obtained by annexing a cell to the left or right of the previously determined stencil. The selected stencil is the one in which the kth difference is smaller in magnitude:

$$j^{k+1}(i) = \begin{cases} j^k(i) - 1, & \text{if } \left|\Delta_L^k\bar{U}\right| < \left|\Delta_R^k\bar{U}\right| \\ j^k(i), & \text{otherwise} \end{cases} \tag{6}$$

where $\Delta_L^k\bar{U}$ and $\Delta_R^k\bar{U}$ are the kth differences obtained, respectively, by annexing a cell to the left or right of the previously determined stencil. Because this algorithm allows the reconstruction stencil to shift freely with the detection of any numerical gradient, it will be referred to as freely adaptive.

Rogerson and Meilberg[3] have reported a degeneration of accuracy that can occur when the freely adaptive stencil algorithm in Eq. (6) is used. Shu[4] has suggested that the algorithm in Eq. (6) be modified to bias the reconstruction stencil toward one that results in a linearly stable scheme. For present purposes, the desired reconstruction stencils are centered if n is odd and one cell upwind if n is even. In this manner, the resulting schemes have an upwind biased flux, as shown for the cases $n = 3$ and 4 in Fig. 1.

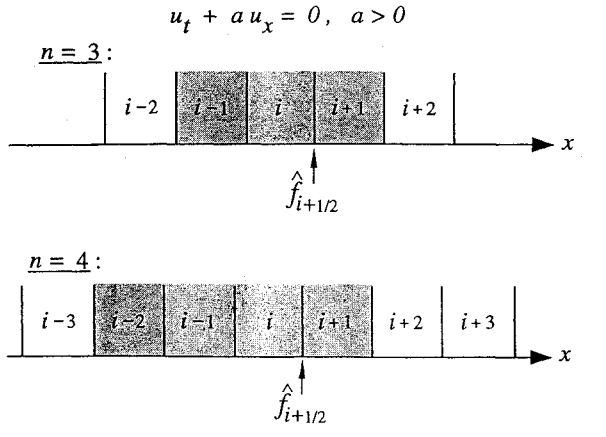

Fig. 1 Preferred reconstruction stencils that result in fluxes that are a) one-half cell upwind and b) one cell upwind.

This biasing can be accomplished by implementing a factor σ in the stencil search in Eq. (6)

$$j^{k+1}(i) = \begin{cases} j^k(k) - 1, & \text{if } \sigma_L\left|\Delta_L^k\bar{U}\right| < \sigma_R\left|\Delta_R^k\bar{U}\right| \\ j^k(i), & \text{otherwise} \end{cases} \tag{7a}$$

where $(\sigma_L, \sigma_R) = (1, \bar{\sigma})$ or $(\bar{\sigma}, 1)$, for biasing to the left or right, respectively, with $\bar{\sigma} > 1$. For Δx sufficiently small, the biased stencil algorithm in Eq. (7a) will yield the desired linearly stable stencil in any smooth region where the kth derivative of the solution is nonzero.

To affect biasing toward linearly stable stencils near points where the kth derivative of the solution might vanish, Atkins[5] has suggested that the stencil be biased toward the linearly stable one wherever the local differences are small. This philosophy is implemented for present purposes as

$$\begin{aligned}&\text{if} \quad \left|\Delta_L^k\bar{U}\right| < \epsilon \quad \text{and} \quad \left|\Delta_R^k\bar{U}\right| < \epsilon \\ &\text{then} \quad j^{k+1}(i) = j_S^{k+1}(i)\end{aligned} \tag{7b}$$

where ϵ is a small parameter and $j_S^k(i)$ identifies the stencil obtained by annexing the kth cell in the linearly stable direction. This additional biasing is particularly important when solving problems that develop regions in which the solution is constant.[5,6] Because these biasing parameters are fixed relative to the solution, the stencil algorithm in Eqs. (7a) and (7b) will be referred to as "linear biasing."

Nonlinear Stencil Biasing

Although the preceding stencil-biasing methods have proven effective for smooth problems, they can give rise to spurious errors near shocks. (See the shock-vortex interaction in the final section.) Therefore, a nonlinear biasing strategy is suggested to retain the linearly stable stencils in smooth regions, yet allow more freedom near a discontinuity. Consider replacing $\bar{\sigma}$ and ϵ in Eqs. (7a) and (7b) with the following:

$$\bar{\sigma}^k = \bar{\sigma}(1-\theta^k) + \theta^k, \qquad \epsilon^k = \epsilon(1-\theta^k) \tag{8a}$$

where θ^k is a simple switch given by

$$\theta^k = \min\left(1, \alpha\left|\Delta_S^k \bar{U}\right|\right), \qquad \alpha > 0 \tag{8b}$$

where $\Delta_S^k \bar{U}$ denotes the kth difference obtained by annexing a cell in the linearly stable direction. Clearly, the range of θ^k is $0 \le \theta^k \le 1$. For a given value of α, the value $1/\alpha$ is the minimum value of $|\Delta^k \bar{U}|$ at which full switching ($\theta^k = 1$) is desired. Note that by setting $\alpha = 0$ the biasing parameters in Eqs. (8a) and (8b) revert to their constant values in Eqs. (7a) and (7b).

That these modified parameters have the required properties can be shown through a brief asymptotic analysis. Although it is not a requirement, this analysis is made more convenient by the assumption that the computational mesh has uniform spacing h. Wherever the kth derivative of $\bar{U}$ is continuous, for h sufficiently small,

$$\theta^k = \alpha\left|\Delta_S^k \bar{U}\right| = \frac{\alpha}{k!}|\bar{U}^{(k)}(\xi)|h^k, \qquad x_{j_S^k(i)} < \xi < x_{j_S^k(i)+k}$$

where $\bar{U}^{(k)}$ is the kth derivative of $\bar{U}$. This argument is based upon a well-known result from approximation theory. (See, for example, Ref. 8.) Therefore, $\theta^k = \mathcal{O}(h^k)$ in smooth regions. However, near a point at which the kth derivative of $\bar{U}$ is discontinuous, the value of $|\Delta_S^k \bar{U}|$ becomes arbitrarily large, for sufficiently small h. Therefore, near such points, $\theta^k = 1$. Thus, for h sufficiently small, the parameters in Eqs. (8a) and (8b) are related to those in Eqs. (7a) and (7b) by

$$\bar{\sigma}^k = \begin{cases} \bar{\sigma} + \mathcal{O}(h^k), & \text{if } \bar{U}^{(k)} \text{ is continuous} \\ 1, & \text{if } \bar{U}^{(k)} \text{ is discontinuous} \end{cases}$$

and

$$\epsilon^k = \begin{cases} \epsilon + \mathcal{O}(h^k), & \text{if } \bar{U}^{(k)} \text{ is continuous} \\ 0, & \text{if } \bar{U}^{(k)} \text{ is discontinuous} \end{cases}$$

So, in regions where the solution is smooth, the values of these biasing parameters are not significantly different from the linear parameters. Furthermore, near a discontinuity in the solution's kth derivative, the values $\bar{\sigma} = 1$ and $\epsilon = 0$ will cause the biased stencil algorithm in Eqs. (7a) and (7b) to revert to the freely adaptive algorithm in Eq. (6). Hence, stable stencils and therefore design accuracy are preserved in smooth regions while still allowing for maximum shifting near discontinuities. Because these modified parameters depend upon the local solution, stencil biasing based upon the preceding strategy will be referred to as nonlinear biasing.

Shocked Flow in a Nozzle

To demonstrate the properties of the nonlinear biasing strategy described in the previous section, a steady-state shocked flow in a quasi-one-dimensional, converging-diverging nozzle is numerically investigated. The governing equations are

$$\frac{\partial}{\partial t}(AU) + \frac{\partial}{\partial x}[AF(U)] = H(U) \tag{9a}$$

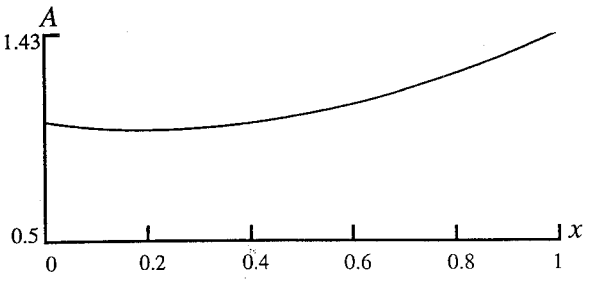

Fig. 2 Nozzle area distribution.

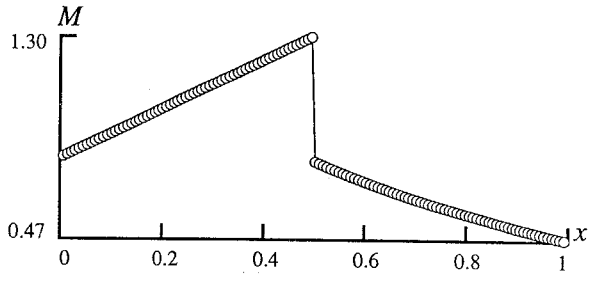

Fig. 3 Mach number distribution.

where

$$U = \begin{bmatrix} \rho \\ \rho u \\ \rho E \end{bmatrix}, \qquad F(U) = \begin{bmatrix} \rho u \\ \rho u^2 + P \\ (\rho E + P)u \end{bmatrix}$$

$$H(U) = \begin{bmatrix} 0 \\ P\dfrac{dA}{dx} \\ 0 \end{bmatrix} \tag{9b}$$

The equation of state is

$$P = (\gamma - 1)\rho\left(E - \tfrac{1}{2}u^2\right)$$

where γ is assumed to have a constant value of 1.4.

The spatial domain of the nozzle is $0 \le x \le 1$, and the flow is oriented from left to right. The flow variables are normalized with respect to upstream stagnation conditions and the area with respect to the value at the throat. The nozzle shape is determined by requiring a linear distribution of Mach number from $M = 0.8$ at the inlet to $M = 1.8$ at the exit, when the flow is isentropic and fully expanded. The resulting area distribution $A(x)$ is illustrated in Fig. 2.

Given the prescribed area distribution, the Mach 0.8 inflow state is retained at $x = 0$, and the outflow condition at $x = 1$ is determined such that a shock forms at $x_s = 0.5$, which corresponds to a preshock Mach number of $M = 1.3$. A steady-state solution is obtained by implementing a third-order ($n = 3$) ENO scheme until residuals are driven to machine zero. The nonlinear stencil biasing in Eqs. (8a) and (8b) are implemented with $\bar{\sigma} = 2, \epsilon = 0.001$, and $\alpha = 2$. Figure 3 depicts the solution, with respect to Mach number, on a uniform mesh of 128 cells.

One of the simpler methods of determining the error of this solution relies on the fact that the value of the entropy-like quantity P/ρ^γ is piecewise constant:

$$S \equiv \frac{P}{\rho^\gamma} = \begin{cases} S_{-\infty}, & x < x_s \\ S_\infty, & x > x_s \end{cases}$$

The subscripts of S denote the preshock and postshock stagnation values. This quantity is plotted in Fig. 4. The pointwise entropy error for this solution on four successively refined meshes is illustrated in Fig. 5. Clearly, the accuracy is third order on either side of the shock, as demonstrated by the error data tabulated in Table 1. The errors $\|e\|_1$ and $\|e\|_\infty$ are, respectively, the average (L_1) error and the maximum (L_∞) error. The number n_c is the computational order of accuracy that is computed from these errors.

Table 1 Entropy errors

	ENO-3-3			
Cells	$\|e\|_1$	n_c	$\|e\|_\infty$	n_c
32	1.479E-05	—	1.554E-04	—
64	1.854E-06	3.00	2.457E-05	2.66
128	2.293E-07	3.02	3.503E-06	2.81
256	2.820E-08	3.02	4.689E-07	2.90

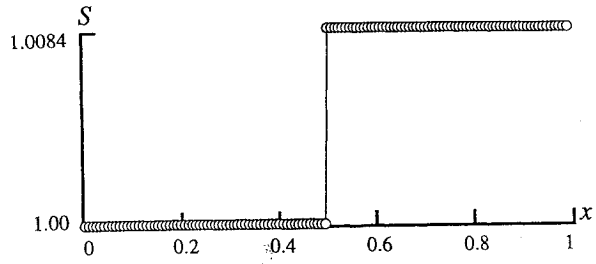

Fig. 4 Entropy distribution.

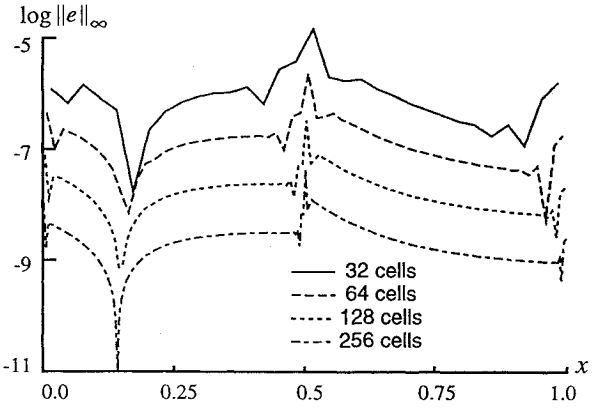

Fig. 5 Entropy error for a shocked nozzle flow.

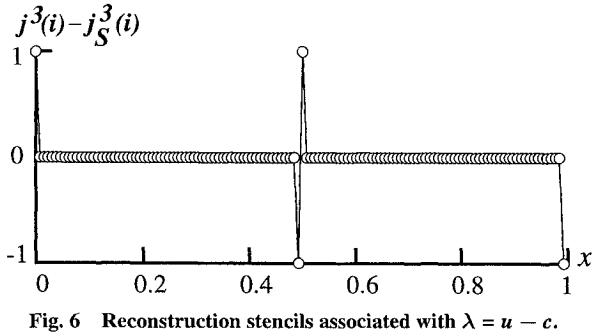

Fig. 6 Reconstruction stencils associated with $\lambda = u - c$.

The accuracy results in Fig. 5 and Table 1 suggest that the nonlinear biasing strategy has the same effect as linear biasing in the smooth regions of this solution. Figure 6 supports this conclusion. The ordinate variable plotted in Fig. 6 is the stencil offset $j^3(i) - j_S^3(i)$, where $j_S^3(i) = i - 1$, as previously shown in Fig. 1. The values -1, 0, or 1 represent a left-shifted, centered, or right-shifted reconstruction stencil, respectively. The stencils represent those used for the reconstruction of the characteristic variable associated with $\lambda = u - c$, on a uniform mesh of 128 cells. (The reconstruction is based on characteristic variables.[1]) As predicted in the analysis of the previous section, the stencils are centered everywhere except near the shock and the boundaries where the stencils are forced to the interior.

Because of the time-independent nature of this case, these results could have been obtained with the linear stencil-biasing strategy. However, an unsteady case, such as a sound-shock interaction, is more difficult to analyze with respect to error. Such a test case is the topic of current research.[9] The differences between the biasing strategies is demonstrated in an unsteady test case in the next section.

Shock-Vortex Interaction

The previous example motivates the study of a more complicated problem, that of an interaction of a vortex with a shock in an axisymmetric flow. The governing equations are

$$\frac{\partial}{\partial t}(rU) + \frac{\partial}{\partial x}(rF) + \frac{\partial}{\partial r}(rG) = H \tag{10a}$$

where

$$U = \begin{bmatrix} \rho \\ \rho u \\ \rho v \\ \rho E \end{bmatrix}, \qquad F = \begin{bmatrix} \rho u \\ \rho u^2 + P \\ \rho uv \\ (\rho E + P)u \end{bmatrix} \tag{10b}$$

$$G = \begin{bmatrix} \rho v \\ \rho uv \\ \rho v^2 + P \\ (\rho E + P)v \end{bmatrix}, \qquad H = \begin{bmatrix} 0 \\ 0 \\ P \\ 0 \end{bmatrix} \tag{10c}$$

The equation of state is

$$P = (\gamma - 1)\rho\left[E - \tfrac{1}{2}(u^2 + v^2)\right]$$

where $\gamma = 1.4$.

The physical problem is described with respect to the (x, r, θ) coordinate system, where the x axis coincides with the axis of symmetry. The initial conditions are implemented in two steps. First, a steady normal shock is positioned on the surface defined by $x = x_s$, with a flow parallel to the axis of symmetry and a preshock Mach number $M = 1.3$. At $t = 0$, a toroidal vortex is imposed upstream of the shock. The vortex is taken from Lamb[10] and augmented with a solid-body filament core of radius δ. Outside the core radius, the velocity induced by the vortex at a point Q in the $x-r$ plane is derived from the stream function

$$\Psi = \frac{-\kappa}{8\pi}\left(d_1^2 + d_2^2\right)\int_0^\pi \left[\frac{1}{E(d_1, d_2, \phi)} - 2E(d_1, d_2, \phi)\right] d\phi \tag{11}$$

where

$$E(d_1, d_2, \phi) = d_1^2 \cos^2(\phi/2) + d_2^2 \sin^2(\phi/2)$$

where the distances d_1 and d_2 are measured from Q to the core center points that lie in the $x-r$ plane, as pictured in Fig. 7. At any point within the core, the velocity is obtained from the value of Ψ when $d_1 = \delta$. The strength of the velocity field induced by this vortex is determined by setting $\kappa = 0.001 u_L$, where u_L is the steady preshock flow speed.

Equations (10a–10c) are solved in the upper half $x-r$ plane on a domain $\{a \le x \le b\} \times \{0 \le r \le R\}$. All flow variables are normalized with respect to the static conditions upstream of the steady shock. The values $b - a$ and R are made large enough relative to the

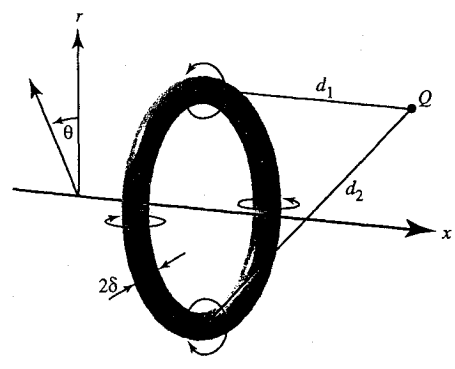

Fig. 7 Toroidal vortex core.

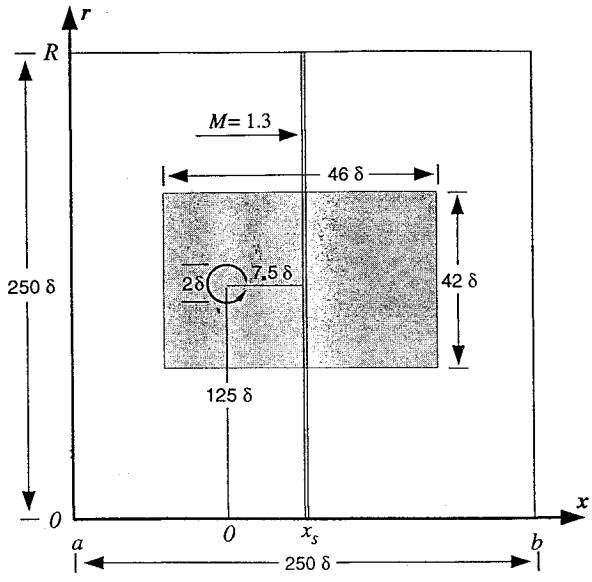

Fig. 8 Diagram for initial conditions (not to scale). Shading denotes fine-grid interaction zone.

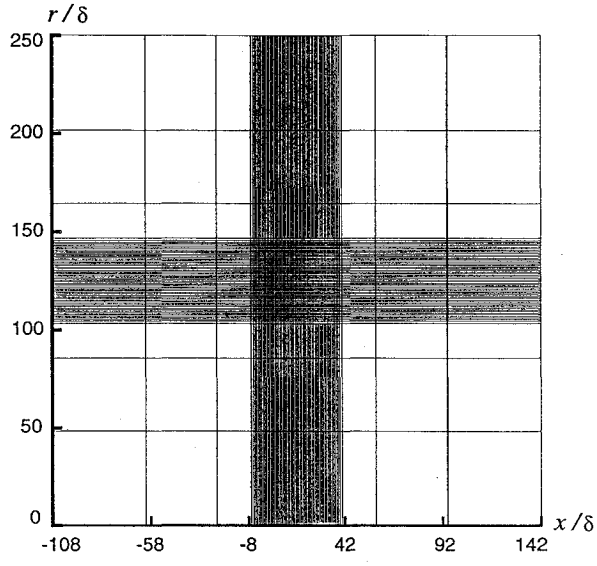

Fig. 9 Computational grid (every fourth point).

vortex strength to neglect the effects of the interaction at the boundaries. Nonreflecting conditions[11] are applied at the inflow ($x = a$) and outflow ($x = b$) boundaries, fluxes are zeroed on the axis of symmetry, and tangency is enforced along the boundary $r = R$.

The vortex is initially positioned such that the center of the filament core is 7.5δ upstream of x_s and 125δ from the axis of symmetry. At this distance from the axis, the filament core can be assumed to have a circular cross section. An interaction zone is predetermined, within which all interesting details of the solution are resolved on a fine computational mesh, as shown in Fig. 8. The computational mesh is 256 × 236 and is composed of a uniform interior region that is smoothly connected to an outer stretched region. The interior interaction zone has mesh spacing $\Delta x = \Delta r = \delta/5$. Every fourth point of this mesh is plotted in Fig. 9.

For $t > 0$, the vortex convects downstream and passes through the shock, at which point the most significant part of the interaction occurs. The shape of the shock is distorted, the vortex strength is altered by the postshock state, and an acoustic wave is produced. This interaction is depicted in Figs. 10a–10c. The numerical scheme implemented here is a third-order two-dimensional finite volume ENO scheme[10] with the freely adaptive stenciling algorithm in Eq. (6). The range of 50 equally spaced pressure contours is restricted to enhance the visualization. The unit of time for these figures is

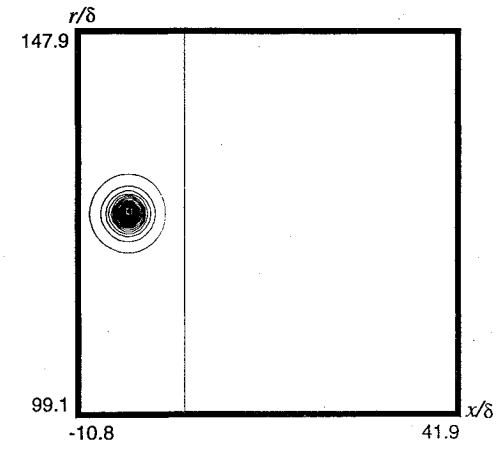

Fig. 10a Pressure, $t = 0$ and $0.994 < P < 1.000$.

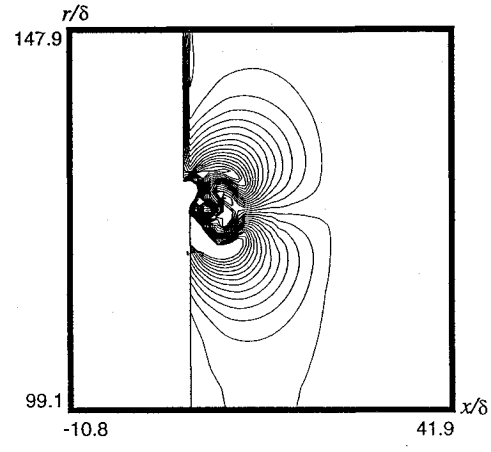

Fig. 10b Pressure, $t = 12T_\delta$ and $1.792 < P < 1.813$.

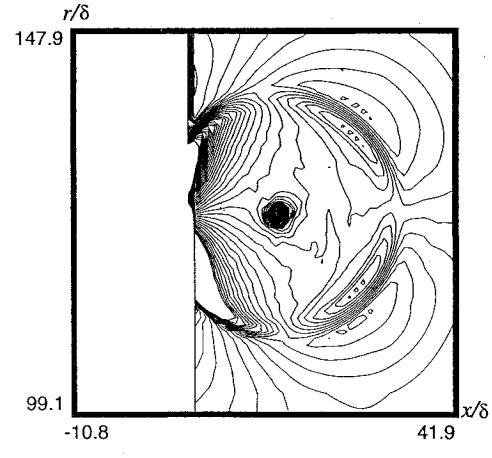

Fig. 10c Pressure, $t = 24T_\delta$ and $1.792 < P < 1.813$.

$T_\delta = \delta/u_L$. As in the previous example, the focus of the present discussion is the numerical algorithm. A discussion of this problem with respect to the physics of sound generation will appear in a future paper.

To test the effects of stencil biasing on this interaction, the solution is examined at $t = 10T_\delta$, after the entire filament core has emerged downstream of the shock. Figure 11a shows a restricted range of pressure contours on a confined area within the interaction zone. Again, the numerical scheme is implemented with freely adaptive stencils. The streamwise reconstruction stencils for the characteristic variable associated with the eigenvalue $\lambda = u + c$ are plotted in Fig. 11b. The shading in this figure represents the three possible values of the stencil offset $j^3(i) - j_S^3(i)$. The stencils vary greatly when allowed to adapt freely, particularly in a case such as this where only small gradients are present in an otherwise uniform region. Of

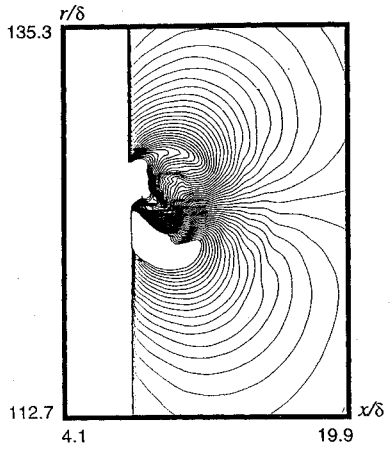

Fig. 11a Pressure, $t = 10T_\delta, 1.792 < P < 1.813$, freely adaptive stenciling, $\bar{\sigma} = 1$, $\epsilon = 0$, and $\alpha = 0$.

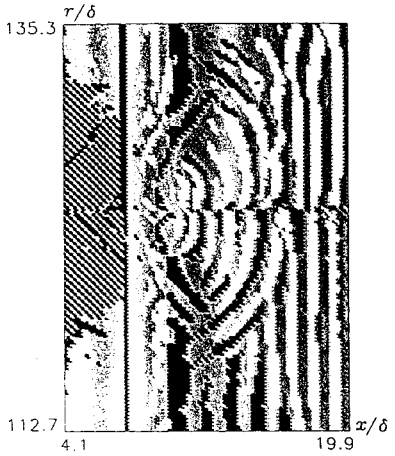

Fig. 11b Reconstruction stencils associated with $\lambda = u + c$ for the solution in Fig. 11a. The values of $j^3(i) - j_S^3(i)$ are -1 for black, 0 for grey, and 1 for white.

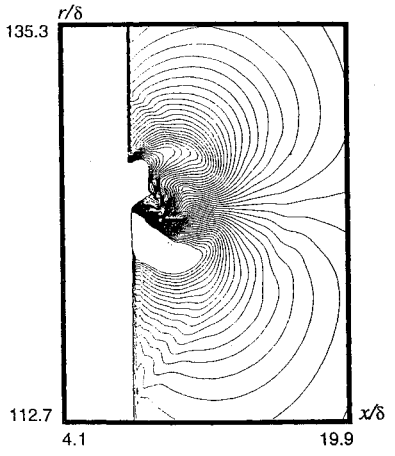

Fig. 12a Pressure, $t = 10T_\delta, 1.792 < P < 1.813$, linear-biased stenciling, $\bar{\sigma} = 2$, $\epsilon = 0.001$, and $\alpha = 0$.

particular concern are the white regions in which the stencil offset is 1, which represents a downwind-shifted stencil for this characteristic variable. Although the calculation for this particular test case does not appear to be adversely affected, previous research[3,4,6] indicates that when linearly unstable stencils are continuously used over the duration of a calculation, accuracy can be severely compromised. The objective here is the development of a robust numerical shock-capturing scheme that can be used for a variety of CAA problems that involve shocks. Therefore, an attempt to bias the stencils is examined.

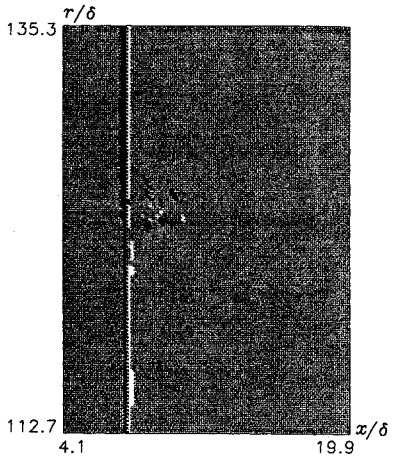

Fig. 12b Reconstruction stencils associated with $\lambda = u + c$ for the solution in Fig. 12a. The values of $j^3(i) - j_S^3(i)$ are -1 for black, 0 for grey, and 1 for white.

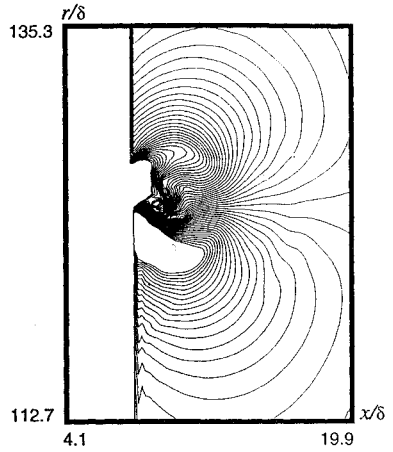

Fig. 13a Pressure, $t = 10T_\delta, 1.792 < P < 1.813$, nonlinear-biased stenciling, $\bar{\sigma} = 2$, $\epsilon = 0.001$, and $\alpha = 2$.

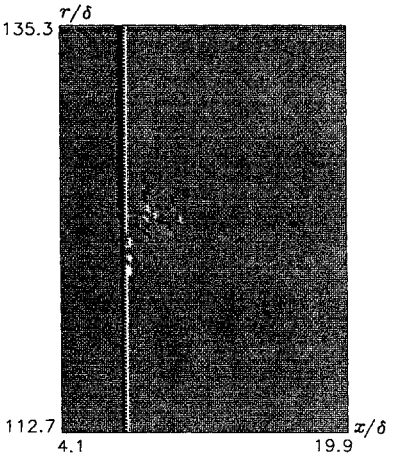

Fig. 13b Reconstruction stencils associated with $\lambda = u + c$ for the solution in Fig. 13a. The values of $j^3(i) - j_S^3(i)$ are -1 for black, 0 for grey, and 1 for white.

In Fig. 12a, spurious waves above and below the filament core appear to the right of the shock when the scheme is applied with linear stencil biasing in Eq. (7) with $\bar{\sigma} = 2$, $\epsilon = 0.001$, and $\alpha = 0$. However, the reconstruction stencils in Fig. 12b are centered in the smooth regions as desired. Figures 13a and 13b depict the pressure field and stencils obtained with the nonlinearly biased stencil algorithm in Eqs. (7) and (9) with $\bar{\sigma} = 2$, $\epsilon = 0.001$, and $\alpha = 2$. The spurious wave that appears in Fig. 12a is only slightly visible beneath the vortex in Fig. 13a. Also, the reconstruction stencils are

centered (i.e., stable) everywhere except near the shock and the vortex filament core. This result indicates that the nonlinear biasing of stencils makes ENO schemes more robust with regard to aeroacoustic applications that involve shocks.

Concluding Remarks

The control of the adaptive stenciling employed in high-order accurate ENO schemes is essential for aeroacoustic applications. The modifications that have been suggested by other authors[4,5] in regard to the biasing of stencils toward those that are linearly stable have been demonstrated to serve their purpose in smooth regions of a flow. However, the numerical study of a shock-vortex interaction has shown that this type of linear biasing can cause errors near moving shocks. A nonlinear biasing strategy has been suggested to allow a freer stencil adaptation near a moving discontinuity than is allowed by the use of constant biasing parameters. In the study of a shocked nozzle flow, this modified stencil biasing was shown to retain linearly stable stencils and therefore design accuracy in smooth regions. This nonlinear stencil biasing was also tested on a shock-vortex interaction and shown to reduce spurious errors in a manner comparable to results obtained with a freely adaptive algorithm, while linearly stable stencils were retained in smooth regions.

Acknowledgment

The first author was supported by the U.S. Government under Contract NASI-19672 while at ViGYAN, Inc., in Hampton, Virginia.

References

[1]Harten, A., Engquist, B., Osher, S., and Chakravarthy, S., "Uniformly High Order Accurate Essentially Non-Oscillatory Schemes III," *Journal of Computational Physics*, Vol. 71, No. 2, 1987, pp. 231–323.

[2]Shu, C., and Osher, S., "Efficient Implementation of Essentially Non-Oscillatory Shock-Capturing Schemes," *Journal of Computational Physics*, Vol. 77, No. 2, 1988, pp. 439–471.

[3]Rogerson, A., and Meiberg, E., "A Numerical Study of the Convergence Properties of ENO Schemes," *Journal of Scientific Computing*, Vol. 5, No. 2, 1990, pp. 151–167.

[4]Shu, C., "Numerical Experiments on the Accuracy of ENO and Modified ENO Schemes," *Journal of Scientific Computing*, Vol. 5, No. 2, 1990, pp. 127–150.

[5]Atkins, H., "High-Order ENO Methods for the Unsteady Navier–Stokes Equations," AIAA Paper 91-1557, June 1991.

[6]Casper, J., Shu, C. W., and Atkins, H., "A Comparison of Two Formulations for High-Order Accurate Essentially Non-Oscillatory Schemes," *AIAA Journal*, Vol. 32, No. 10, 1994, pp. 1970–1977.

[7]Casper, J., and Atkins, H., "A Finite-Volume High-Order ENO Scheme for Two-Dimensional Hyperbolic Systems," *Journal of Computational Physics*, Vol. 106, May 1993, pp. 62–76.

[8]Powell, M. J. D., *Approximation Theory and Methods*, Cambridge Univ. Press, New York, 1981.

[9]Casper, J., and Carpenter, M., "Computational Considerations for the Simulation of Shock-Induced Sound," NASA TM, TM110222, Nov. 1995.

[10]Lamb, H., *Hydrodynamics*, Cambridge Univ. Press, New York, 1932.

[11]Atkins, H., and Casper, J., "Non-Reflective Boundary Conditions for High-Order Methods," *AIAA Journal*, Vol. 32, No. 3, 1994, pp. 512–518.